AIAA JOURNAL
Vol. 36, No. 8, August 1998

Particle Image Velocimetry via Wavelet Analysis

Jeonghwan Ko,* Andrew J. Kurdila,† Jose L. Gilarranz,‡ and Othon K. Rediniotis§
Texas A&M University, College Station, Texas 77843-3141

Novel analytical and image processing methods derived as part of the development of a digital particle image velocimetry system, based on multiresolution analysis, are presented. The derivation of wavelet-based multiresolution methods for velocity field reconstruction is addressed, and the experimental setup used for validation of results is described. New techniques are proposed with improved spatial resolution and reliability over some existing methods. The techniques are based on wavelet-based representations of digital particle image data that are used to calculate spatially localized and frequency localized filtered correlations of successive images. An essential feature of the method is the development of windowed cross-correlation expressions for wavelet-based expansions that are not orthogonal (or biorthogonal) over the cross-correlation window. The methodology makes use of recently introduced refinable functions and generalized connection coefficients derived in wavelet-based finite element methods. A conventional charge-coupled device camera is used with a frame rate of 30 frames/s and pixel resolution of 512 × 480 per frame. The images are acquired in pairs at 30 frames/s, with a user-defined time delay between image pairs, to capture the flowfield structure evolution. The flow illumination was achieved using a 5-W, argon-ion laser. Finally, hardware and algorithm performance is demonstrated via sample water-tunnel experiments.

I. Introduction

OPTICAL measurement techniques in fluid mechanics encompass a wide spectrum of methods ranging from point interrogations (laser Doppler velocimetry) to planar imaging [particle image velocimetry (PIV) and particle tracking velocimetry (PTV)] to volumetric investigations (three-dimensional PIV and three-dimensional PTV). In recent years, much attention has been given to planar and three-dimensional flowfield interrogation methods. Specifically, PIV has been widely accepted and applied while also undergoing continual advancement.

PIV has proven to be a useful technique for temporally characterizing nonperiodic and quasiperiodic phenomena for which accurate phase referencing is not available. Lack of phase referencing rules out the use of point measurement and ensemble averaging techniques to extract temporal information on the flow and perform space–time cross correlations. However, on occasion, the vector fields generated with the use of this method may present a certain number of erroneous vectors, which may be related to certain factors, such as poor quality of images, low seeding particle density in the image, large displacements of particles between consecutive images, i.e., high-velocity flows, etc. Furthermore, the type of image processing algorithms that are used for the data reduction process may play an important role in the quality of the resultant vector field. To resolve this last issue, improved and novel image processing algorithms are presented herein. A brief review of representative research in PIV follows.

Processing of PIV images has received significant attention in terms of improving method reliability and reducing computation time. The processing of PIV images can be done either digitally or optically. For typical digital PIV (DPIV) analysis, the image is either acquired in digital form [charge-coupled device (CCD) camera and frame-grabber hardware] or acquired in analog form (photography) and subsequently digitized using optical scanning techniques and hardware. It is then stored as a numerically equivalent image file and is manipulated and analyzed using computational algorithms, most often based on autocorrelation, cross-correlation, and particle tracking techniques. Grant and Liu[1] used an autocorrelation method to analyze multiexposed PIV images. Interrogation windows are shifted within the image to determine where the correlation in particle displacement is highest, thereby determining analytically the average velocity of the flow in that region. Cross-correlation techniques have been shown to improve the performance of PIV systems.[2–4] Willert and Gharib[3] utilized a CCD camera that immediately provides images in digital format. Utilizing two consecutive images, a local spatial cross correlation, in Fourier space, is performed between the two images to resolve the velocity distribution along a plane. Shimada et al.[4] further developed Fourier transform-based image processing methods using normalization and spatial filtering. The normalization and filtering incorporated alternative Fourier transform kernels, which resulted in the emphasis of low-frequency information. In addition, other types of filtering[5,6] can allow for more refined data extraction and rapid data reduction.

Optical processing techniques are often used to remove the requirement to digitize the images and to alleviate the computational burden. For quantitative processing, PIV images have often been scanned by a laser to produce a series of Young's fringe patterns, which can be locally analyzed to derive the corresponding two-dimensional velocity vectors. This method requires direct pointwise interrogations of the film to analyze the local resulting Young's fringe pattern. Arnold and Hinsch[7] developed an optical parallel processing method that uses an array of holographically produced interrogation beams. Analysis of the resulting array of Young's fringe patterns results in the position-resolved velocity field. Optical filtering methods[8,9] have also been developed that speed up the image processing.

Both the digital autocorrelation methods and the optical processing techniques do not inherently reveal information about the velocity direction. Several methods have been developed to remove the directional ambiguity associated with some PIV processing methods. Pulse tagging, used by Grant and Liu,[10] employs two different and distinct light pulse durations in multiexposed images. Adrian[11] and Landreth et al.[12] introduced an image shifting technique, which uses a rotating mirror to impose a positive shift corresponding to some finite forward velocity to all image particles. Image shifting[11–14] can be used to offset negative velocities by the imposed forward velocity shift, therefore alleviating any directional ambiguity. A two-color PIV system, developed by Trump et al.,[15] uses a high-resolution color CCD camera. Two colored laser sheets were used for successive illumination of the particles, thereby resolving the directional ambiguity through the color sequence of the particles. Directional ambiguity is not a problem in techniques based on the

---

Received July 3, 1997; revision received March 8, 1998; accepted for publication April 8, 1998.

*Postdoctoral Research Associate, Aerospace Engineering Department. Member AIAA.

†Associate Professor, Aerospace Engineering Department. Member AIAA.

‡Research Assistant, Aerospace Engineering Department. Student Member AIAA.

§Assistant Professor, Aerospace Engineering Department. Member AIAA.

cross correlation of two consecutive images.[3] This method is emphasized herein.

For fast-varying flows with fine spatial structure, traditional PIV approaches fail to capture the small time and length scales of the flowfield and their temporal–spatial evolution. Their capture is necessary to address issues such as transient response of both the fluid and the structure during rapid fluid–structure interactions or the energy transfer process among the different scales in transition and turbulence. Therefore, to resolve these issues, the use of high-speed cameras, with frame rates of up to 10,000 frames/s and high image resolutions are deemed necessary. Gilarranz et al.[16] developed a high-frame-rate, high-resolution cinematographic PIV system, which combined the use of a high-speed, high-resolution film camera (with frame rates up to 10,000 frames/s and a resolution of about 1400 × 1000 pixels per frame) with the use of novel image processing techniques with improved spatial resolution and reliability. Similar to the work presented in Ref. 16, Vogel and Lauterborn[17] used high-speed photography to get time-resolved flow information around cavitation bubbles during their collapse. In view of the inherent computational expense associated with the task of extracting velocity field characterizations from such high-speed cameras operating at equivalent resolutions on the order of 1400 × 1000 pixels, novel windowed, wavelet-based correlation methods are presented in this paper.

A great deal of literature has accumulated over the past five years on wavelet and multiresolution analysis in applications to signal processing. Although hardly exhaustive, representative overviews of the progress in this field can be found in Refs. 18 and 19. Roughly speaking, much of the enthusiasm with regard to the utility of wavelets for applications in signal processing can be attributed to the time-frequency localization properties of these basis systems. As a basis for the representation of functions, wavelets are unique in that they can be tailored to have a designed band-limited frequency content and, simultaneously, can have local support in time. These properties should be contrasted with the classical Fourier basis functions, for example, which are ideally localized in frequency (a single spectral line) but are supported over the entire real line in the time domain. In applications to PIV, the ability to achieve local spatial and frequency filtering provides an automatic process for calculating cross correlation for features at different length scales or particle sizes at distinct physical locations in the flow. In addition, the ability of the wavelet and multiscale representations to yield highly compressed representations of images and operators has been reported by numerous authors (see Ref. 20, for example). This paper derives modifications of the classical cross-correlation functions that are required for windowed wavelet representations. By utilizing the fast wavelet transform to project out coarse features in the PIV data, improved windowed-wavelet cross correlations are obtained.

The remainder of this paper is organized as follows. Section II presents novel particle image cross-correlation algorithms based on wavelet theory. Section III describes the imaging hardware, as well as the components of the experimental setup that was used to generate the data. Section IV includes the description of sample experiments performed to demonstrate the performance of the techniques proposed herein. The discussion of the results may also be found in Sec. IV. Finally, Sec. V includes the concluding remarks of this work.

II. Wavelet-Based Windowed Cross Correlation

A. Conventional Cross Correlation

To motivate the derivation of wavelet-based DPIV algorithms that follow, we briefly review conventional cross-correlation methods as they are applied in DPIV. Typically, instantaneous planar velocity distributions are derived from two captured images separated by a known time interval, by cross correlating corresponding sampling windows in the two images. In typical approaches,[3] the image data from a window (for a 512 × 512 image, a typical window size is 32 × 32 pixels) taken in the first image and that from a window at the same position in the second image are cross correlated. Consider the two consecutive images shown in Fig. 1. We let $f(k,l)$ and $g(k,l)$ represent the pixel intensities (typically 0–255) at pixel locations (k,l) in the first and second images, respectively. From any of a number of texts (see, for example, Ref. 21) treating digital image processing, we find that the discrete cross correlation $R(m,n)$ associated with discrete functions $f(k,l)$, and $g(k,l)$ is given by

$$R(m,n) = \frac{\sum_k \sum_l f(k,l) g(k+m, l+n)}{\sum_k \sum_l f^2(k,l) \sum_k \sum_l g^2(k,l)} \tag{1}$$

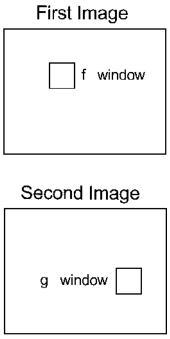

Fig. 1 Interrogation windows in two consecutive images.

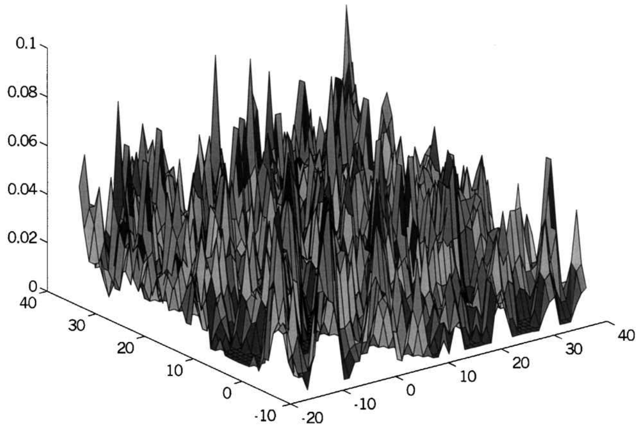

Fig. 2 Cross-correlation plot for a 16 × 16 interrogation window.

In this expression, the function $R(m,n)$ measures the correlation of the discrete functions $f(k,l)$ and $g(k,l)$ when they are relatively shifted by (m,n) pixels. We do not explicitly express the limits of summation, as this will clearly depend on the window size and location. The location of the cross-correlation peak gives the mean displacement of the particles in the interrogation window. This process is repeated by moving the window until the entire image is covered. In Ref. 3, inaccuracies are introduced because the window in the second image is at the same location as the window in the first image. This could yield erroneous predictions because some of the particles in the first window could, due to their finite velocity, move outside of the interrogation window. The likelihood of erroneous predictions of the particle displacement grows as the flow velocity or, equivalently, the displacement increases. Moreover, the successful performance of the cross correlation requires the use of a rather large interrogation window, typically 32 × 32 pixels. The algorithm returns a single velocity prediction for the entire interrogation window; therefore, all of the points within the window are assumed to have the same uniform velocity, and any spatial velocity gradients within the window are missed altogether. This restriction can be somewhat alleviated by overlapping the interrogation windows. In general, for a 512 × 512 image, the velocity map has a grid size of 16 × 16. This resolution is inadequate when fine length scales are to be resolved. An idea of the effects of noise and measurement imprecision is shown in Fig. 2, which presents a typical windowed cross correlation plotted for two consecutive images. The determination of a local maximum is clearly difficult without significant filtering. In the next section, we will show how the use of wavelet bases can be used to generate a family of expressions similar to Eq. (1) but depending on a choice of wavelet and on a class of filter operations.

B. Basics of Wavelet Theory

A detailed discussion of the theory of wavelets and multiresolution analysis is, of course, beyond the scope of this paper. In this section, we summarize just enough of the relevant theory to explain the PIV methodologies presented later. The interested reader is referred to any of the numerous recent texts, such as the work of Daubechies,[22] for a thorough discussion of wavelet and multiresolution analysis. To derive the appropriate wavelet-based correlation functions for images in two dimensions, we first define wavelets and multiresolution functions on the real line $\Re$. The extension to two-dimensional images is discussed subsequently. We approximate a given function $f(x)$ via a representation in the terms of functions $\phi_{J,k}(x)$:

$$f(x) \approx f^J(x) = \sum_{k \in N} \alpha_{J,k}\phi_{J,k}(x) \tag{2}$$

where J defines the finest mesh resolution $h = 2^{-J}$ and $\phi_{J,k}(x)$ is a family of basis functions defined as

$$\phi_{J,k}(x) \equiv 2^{J/2}\phi(2^J x - k), \qquad \forall k \in N \tag{3}$$

Carefully note that the basis functions $\phi_{J,k}(x)$ are defined as dilates and translates of the single function $\phi(x)$, the scaling function of a multiresolution analysis. The number and variety of scaling functions derived over the past few years has increased enormously, and the properties of scaling functions vary considerably among different types. In this paper, we will make rather restrictive assumptions on $\phi(x)$. These assumptions simplify the discussions in Sec. II.C but are by no means required for the techniques outlined in this paper to be applied using more general classes of scaling functions and wavelets. We assume the following.

1) The function $\phi(x)$ has compact support, i.e., vanishes outside a closed bounded set.

2) The functions $\phi_{J,k}(x)$ form an orthonormal set of functions over $L^2(R)$, i.e.,

$$\int_R \phi_{J,k}(x)\phi_{m,n}(x)\,\mathrm{d}x = \delta_{(J,k),(m,n)}$$

3) The function $\phi(x)$ satisfies a scalar two-scale equation with some finite sequence h_k:

$$\phi(x) = \sum_{k \in S} h_k \phi(2x - k) \tag{4}$$

In Eq. (4), h_k is the mask, or low-frequency filter, characterizing the scaling function. An important consequence of the third assumption, however, is that the scaling functions $\phi_{J,k}(x)$ can be used to construct nested spaces. If we define

$$V_J = \mathrm{span}\{\phi_{J,k}\}_{k \in N}, \qquad V_{J-1} = \mathrm{span}\{\phi_{J-1,k}\}_{k \in N} \tag{5}$$

it is clear from Eq. (4) that we have

$$V_{J-1} \subseteq V_J \tag{6}$$

Each of these assumptions can be weakened; we can consider scaling functions with infinite support, scaling functions that satisfy vector-valued matrix refinement equations, or scaling functions that yield bases $\phi_{J,k}(x)$ that are not orthogonal. From the scaling function $\phi(x)$, we define the wavelet $\psi(x)$ associated with a multiresolution analysis according to

$$\psi(x) = \sum_{k \in S'} g_k \phi(2x - k) \tag{7}$$

By a careful definition of the mask coefficients g_k in terms of the h_k, it is possible to show[22] that

$$W_J = \mathrm{span}\{\psi_{J,k}\}_{k \in N} \tag{8}$$

where

$$\psi_{J,k}(x) = 2^{J/2}\psi(2^J x - k) \tag{9}$$

is the orthogonal complement of V_J in V_{J+1}. That is,

$$\begin{aligned} \underset{\substack{\text{fine mesh}\\ \text{approx. space}}}{V_{J+1}} &= \mathrm{span}\{\phi_{J+1,k}\} = \mathrm{span}\{\phi_{J,k}\} \oplus \mathrm{span}\{\psi_{J,k}\} \\ &= \underset{\substack{\text{coarse mesh}\\ \text{approx. space}}}{V_J} \oplus \underset{\substack{\text{detail}\\ \text{approx. space}}}{W_J} \end{aligned} \tag{10}$$

With these observations, we can write the single-scale expansion in terms of a multiscale expansion:

$$\begin{aligned} f^J(x) &= \sum_k \alpha_{J-1,k}\phi_{J-1,k}(x) + \sum_s \beta_{J-1,s}\psi_{J-1,s}(x) \\ &= \sum_k \alpha_{J-2,k}\phi_{J-2,k}(x) + \sum_s \beta_{J-2,s}\psi_{J-2,s}(x) \\ &\quad + \sum_s \beta_{J-1,s}\psi_{J-1,s}(x) \end{aligned} \tag{11}$$

By induction, we obtain

$$f^J(x) = \sum_k \alpha_{M,k}\phi_{M,k}(x) + \sum_{m=M}^{J-1}\sum_s \beta_{m,s}\psi_{m,s}(x) \tag{12}$$

The decomposition and reconstruction between different levels of discrete coefficients $\{\alpha_{j,k}\}$ and $\{\beta_{j,k}\}$ are performed through fast wavelet transforms utilizing the two filters $\{h_k\}$ and $\{g_k\}$ defined in Eqs. (4) and (7) (Ref. 22). The scaling function part of the multilevel expression in Eq. (12) contains low-frequency or large-scale information, and the wavelet components represent high-frequency or small-scale information of the original function.

With the construction of the multiresolution analysis in one dimension in Eq. (12), it is not difficult to extend the analysis to two dimensions via tensor products. That is, if we define

$$\begin{aligned} \Phi(x,y) &= \phi(x)\phi(y) \\ \Psi^1(x,y) &= \phi(x)\psi(y) \\ \Psi^2(x,y) &= \psi(x)\phi(y) \\ \Psi^3(x,y) &= \psi(x)\psi(y) \end{aligned} \quad \text{and} \quad \begin{aligned} V_J &= \mathrm{span}\{\Phi_{J,(k,l)}\}_{(k,l)\in N\times N} \\ W_J^i &= \mathrm{span}\{\Psi^i_{J,(k,l)}\}_{(k,l)\in N\times N} \end{aligned}$$

$$i = 1, 2, 3 \tag{13}$$

we can show that

$$\underset{\substack{\text{fine mesh}\\ \text{approx.}\\ \text{space}}}{V_{J+1}} = \underset{\substack{\text{coarse mesh}\\ \text{approx.}\\ \text{space}}}{V_J} \oplus \underset{\substack{\text{vertical}\\ \text{detail}\\ \text{approx.}\\ \text{space}}}{W_J^1} \oplus \underset{\substack{\text{horizontal}\\ \text{detail}\\ \text{approx.}\\ \text{space}}}{W_J^2} \oplus \underset{\substack{\text{diagonal}\\ \text{detail}\\ \text{approx.}\\ \text{space}}}{W_J^3} \tag{14}$$

for the multiresolution analysis of two-dimensional spaces. Later, we utilize the preceding decomposition for denoising and extracting detail features of particle images obtained from experiments. It is emphasized that the wavelet decomposition is one of the two major procedures in our current methodology.

C. Wavelet- and Multiresolution-Based Cross Correlations

In this section, we discuss the derivation of windowed cross-correlation methods from wavelet-based representations of the digitized particle images. To provide motivation for the methodology discussed in this section, consider the one-dimensional version of the conventional discrete correlation

$$R(m) = \frac{\sum_{k=-\infty}^{+\infty} f_k g_{k+m}}{\sum f_k^2 \sum g_k^2} = \frac{\tilde{R}(m)}{\|f\|^2\|g\|^2} \tag{15}$$

where the norms $\|f\|$ and $\|g\|$ are calculated over the sample window. To simplify the form of the equations that follow, we will utilize $R(\cdot)$ to denote the normalized cross correlation and $\tilde{R}(\cdot)$ to denote unnormalized cross correlation. This equation can be derived by assuming that we have been given discrete values of two functions $f(x)$ and $g(x)$ and have represented these functions via approximations having the form

$$f^J(x) = \sum_{k=0}^{N-1} f_{J,k}\phi_{J,k}(x) \tag{16}$$

and

$$g^J(x) = \sum_{k=0}^{N-1} g_{J,k}\phi_{J,k}(x) \tag{17}$$

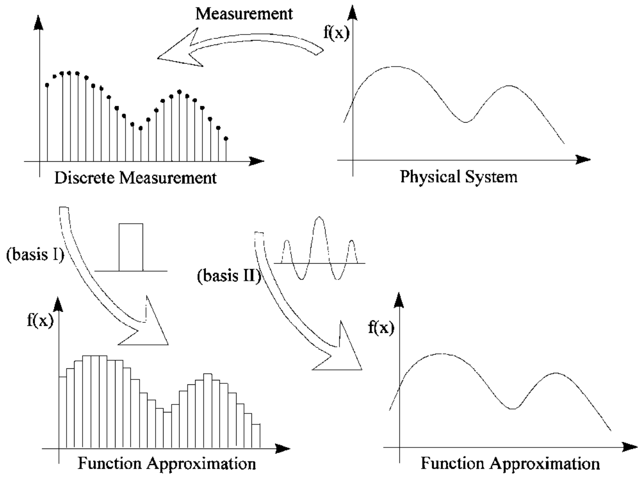

Fig. 3 Approximation of discrete data by an analytic function in terms of different bases.

where the basis functions $\phi_{J,k}(x)$ are simply the step functions

$$\phi_{J,k}(x) = \begin{cases} 1, & 2^{-J}k \le x \le 2^{-J}(k+1) \\ 0, & \text{otherwise} \end{cases} \tag{18}$$

This situation is shown schematically in Fig. 3. It is assumed that the physical data to be measured are represented by some unknown function $f(x)$ that is not necessarily discrete.

Via measurement, we obtain discrete data that can be used directly to represent a piecewise constant approximation of the function. Of course, this is only one of many possible choices for representing the function. In fact, it is not difficult to show that the discrete cross correlation in Eq. (15) is valid for any functions having the form shown in Eqs. (16) and (17) whenever 1) the basis functions $\{\phi_{J,k}\}_{k\in N}$ form an orthonormal system and 2) the basis functions $\{\phi_{J,k}\}_{k\in N}$ satisfy the translation property, $\phi_{J,k}(x+2^{-J}m) = \phi_{J,k-m}(x)$. If these two properties hold, we can write

$$\begin{aligned} \tilde{R}(2^{-J}\xi) &= \int_{\Re} f^J(x-2^{-J}\xi)g^J(x)\,\mathrm{d}x \\ &= \int_{\Re}\left[\sum_{k=0}^{N-1} f_k\phi_{J,k}(x-2^{-J}\xi)\right]\left[\sum_{m=0}^{N-1} g_m\phi_{J,m}(x)\right]\mathrm{d}x \\ &= \sum_{k=0}^{N-1}\sum_{m=0}^{N-1} f_k g_m \int_{\Re}\phi_{J,k}(x-2^{-J}\xi)\phi_{J,m}(x)\,\mathrm{d}x \end{aligned} \tag{19}$$

so that

$$R(2^{-J}\xi) = \frac{\sum_k f_k g_{k+m}}{\sum f_k^2 \sum g_k^2} \tag{20}$$

The recently derived family of wavelet functions provides a rich collection of functions having precisely the two characteristics just defined. Hence, the cross-correlation expression in Eq. (20) remains valid, without modification, whenever we choose an orthonormal set of wavelet basis functions and the interrogation window is the entire (periodically extended) image.

This observation allows us to express the cross correlation of functions that have been approximated by wavelets and that are defined over the entire real line in the usual fashion. However, for applications to PIV, we are interested in evaluating local cross correlations over a convenient subdomain, or window. In this case, the conventional discrete cross correlation in Eq. (15) remains valid, even over the local window. We need only restrict the indices in the summation over the local window. This windowed correlation procedure works because the step functions in Eq. (18) are orthonormal over grid-aligned rectangular windows. On the other hand, if we allow wavelet bases in the expansions, we encounter difficulties. The wavelet bases, although orthonormal over the entire real line, are not orthogonal when restricted to grid-aligned domains. In other words, when we calculate the windowed cross correlation of functions that have been expanded in terms of orthonormal basis functions, as in

$$\tilde{R}_\Omega(2^{-J}\xi) = \int_\Omega f^J|_\Omega(x-2^{-J}\xi)g^J(x)\,\mathrm{d}x \tag{21}$$

the functions $f^J|_\Omega$ and g^J are not orthogonal over the (window) domain Ω.

The modifications to calculate the windowed cross correlation of functions approximated via wavelet expansions can be achieved using the notion of refinable functions discussed in Refs. 23 and 24. This methodology has also been employed in Ref. 25 for the development of wavelet-based finite element methods. The derivation of the windowed cross correlation is achieved by first noting that the integral over the domain Ω can be expressed as an integral over the entire real line:

$$\begin{aligned} \tilde{R}_\Omega(2^{-J}\xi) &= \int_\Omega f^J|_\Omega(x-2^{-J}\xi)g^J(x)\,\mathrm{d}x \\ &= \int_{\Re} f^J(x-2^{-J}\xi)\mathcal{X}_\Omega(x-2^{-J}\xi)g^J(x)\,\mathrm{d}x \end{aligned} \tag{22}$$

by introducing the characteristic function of the domain Ω

$$\mathcal{X}_\Omega(x) = \sum_{l=0}^{w}\mathcal{X}_{[0,1]}(2^Jx-s-l) \tag{23}$$

where s corresponds to the left boundary of the domain Ω, w is the domain's width, and

$$\mathcal{X}_{[0,1]}(x) = \begin{cases} 1, & x\in[0,1] \\ 0, & \text{otherwise} \end{cases} \tag{24}$$

When we expand the windowed cross correlation in Eq. (22), we obtain

$$\begin{aligned} \tilde{R}_\Omega(2^{-J}\xi) &= \int_{\Re} f^J(x-2^{-J}\xi)\mathcal{X}_\Omega(x-2^{-J}\xi)g^J(x)\,\mathrm{d}x \\ &= \int_{\Re}\left[\sum_k f_k\phi_{J,k}(x-2^{-J}\xi)\right]\left[\sum_l g_l\phi_{J,l}(x)\right] \\ &\times\left[\sum_{m=0}^{w}\mathcal{X}_{[0,1]}(2^Jx-\xi-s-m)\right]\mathrm{d}x = \sum_k\sum_l\sum_{m=0}^{w} f_k g_l \\ &\times\int_{\Re} 2^{J/2}\phi(2^Jx-\xi-k)2^{J/2}\phi(2^Jx-l) \\ &\times\mathcal{X}_{[0,1]}(2^Jx-\xi-s-m)\,\mathrm{d}x \end{aligned} \tag{25}$$

This expression would reduce to the usual, discrete cross correlation if the integrand were equal to the Kronecker delta function. Alternatively, we utilize the change of variables

$$\begin{aligned} &\int_{\Re} 2^{J/2}\phi(2^Jx-\xi-k)2^{J/2}\phi(2^Jx-l)\mathcal{X}_{[0,1]}(2^Jx-\xi-s-m)\,\mathrm{d}x \\ &= \int_{\Re}\phi(x-\xi-k)\phi(x-l)\mathcal{X}_{[0,1]}(x-\xi-s-m)\,\mathrm{d}x \\ &= \int_{\Re}\mathcal{X}_{[0,1]}(x)\phi(x+s+m-k)\phi(x+\xi+s+m-l)\,\mathrm{d}x \end{aligned} \tag{26}$$

and define the three-term connection coefficients to be

$$\begin{aligned} \Gamma^{0,0}_{k-s-m,l-\xi-s-m} &= \int_{\Re}\mathcal{X}_{[0,1]}(x)\phi(x+s+m-k) \\ &\times\phi(x+\xi+s+m-l)\,\mathrm{d}x \end{aligned} \tag{27}$$

The final expression for the windowed cross correlation for functions expressed in terms of wavelet expansions can be written as

$$\tilde{R}_\Omega(2^{-J}\xi) = \sum_k\sum_l\sum_{m=0}^{w} f_k g_l\Gamma^{0,0}_{k-s-m,l-\xi-s-m} \tag{28}$$

At this point, it is important to note the following:

1) The integrals defining $\Gamma^{0,0}_{s,t}$ are not trivial to calculate in general. For many cases of interest, the wavelet scaling functions ϕ comprising the integrals cannot be expressed in closed form.

2) Numerical methods exist for calculating the entries $\Gamma^{0,0}_{s,t}$ to any degree of precision. Techniques for evaluating these integrals are discussed in Refs. 23 and 24.

3) Once the entries of $\Gamma^{0,0}_{s,t}$ have been calculated numerically, they can be stored and applied very rapidly. The number of nonzero entries in $\Gamma^{0,0}_{s,t}$ is proportional to the length of the mask defining the wavelet.

4) The entries of $\Gamma^{0,0}_{s,t}$ are different for different (families of) wavelets.

The set of $\Gamma^{0,0}_{s,t}$ corresponding to the Daubechies wavelets of order 3 were utilized in the present numerical examples. Software for evaluating the $\Gamma^{0,0}_{s,t}$ values for more general families of wavelets is available in Ref. 26.

The expression in Eq. (28) is sufficient, in principle, for calculating the desired windowed cross correlations. If we implement the expression in Eq. (28) directly, however, the time to calculate the cross correlation can be prohibitively long. This fact is particularly true when we extend these results to the case of two-dimensional signals (images). It is possible to improve the efficiency of the cross-correlation calculation via some simple observations. Given a window of the function $f(x)$ that we wish to cross correlate with an entire signal $g(x)$, we can reorganize the calculations as follows:

$$\begin{aligned}\tilde{R}_{\Omega}(2^{-J}\xi) &= \sum_{k}\sum_{l}\sum_{m=0}^{w} f_k g_l \Gamma^{0,0}_{k-s-m,l-\xi-s-m}\\ &= \sum_{l} g_l\left(\sum_{k}\sum_{m=0}^{w} f_k \Gamma^{0,0}_{k-s-m,l-\xi-s-m}\right)\\ &= \sum_{l} g_l M(l-\xi-s)\end{aligned} \tag{29}$$

In the preceding equations, we have defined a new set of quantities

$$M(l-\xi-s) = \sum_{k}\sum_{m=0}^{w} f_k \Gamma^{0,0}_{k-s-m,l-\xi-s-m} \tag{30}$$

Note that these coefficients can be precomputed, given an initial window of the function $f(x)$, and applied as a filter to the coefficients defining the function $g(x)$.

The extension of all of the preceding results via tensor products to obtain formulas appropriate for two-dimensional particle images is straightforward. If we assume that we are given the wavelet approximations

$$\begin{aligned}f^J(x,y) &= \sum_{k}\sum_{n} f_{k,n}\phi_{J,k}(x)\phi_{J,n}(y)\\ g^J(x,y) &= \sum_{l}\sum_{o} g_{l,o}\phi_{J,l}(x)\phi_{J,o}(y)\end{aligned} \tag{31}$$

the windowed cross-correlation expression can be written as

$$\begin{aligned}&\tilde{R}_{\Omega}\left(2^{-J}\xi_1, 2^{-J}\xi_2\right)\\ &= \sum_{k,n}\sum_{l,o}\sum_{m,p}^{w_1,w_2} f_{k,n} g_{l,o} \Gamma^{0,0}_{k-s_1-m,l-\xi_1-s_1-m}\Gamma^{0,0}_{n-s_2-p,o-\xi_2-s_2-p}\\ &= \sum_{l,o} g_{l,o}\left(\sum_{k,n}\sum_{m,p}^{w_1,w_2} f_{k,n}\Gamma^{0,0}_{k-s_1-m,l-\xi_1-s_1-m}\Gamma^{0,0}_{n-s_2-p,o-\xi_2-s_2-p}\right)\\ &= \sum_{l,o} g_{l,o} M(l-\xi_1-m, o-\xi_2-s_2-p)\end{aligned} \tag{32}$$

In Eq. (32), we have introduced the doubly indexed set of coefficients

$$\begin{aligned}&M(l-\xi_1-s_1-m, o-\xi_2-s_2-p)\\ &= \sum_{k,n}\sum_{m,p}^{w_1,w_2} f_{k,n}\Gamma^{0,0}_{k-s_1-m,l-\xi_1-s_1-m}\Gamma^{0,0}_{n-s_2-p,o-\xi_2-s_2-p}\end{aligned} \tag{33}$$

that must be precomputed for each window of the function $f(x, y)$.

III. Description of Imaging Hardware and Experimental Setup

To acquire the images used to test the performance of the image processing algorithms proposed herein, we utilized a Pulnix TM-9701 CCD camera with a frame rate of 30 frames/s, a variable internal electronic shutter, and a sensing element array with a resolution of 512 × 480 pixels. The CCD camera is interfaced to a personal computer with a Data Translation DT 2861 frame-grabber and software that enables the user to save the images in various formats. To resolve the desired length scales, the proper zoom level was obtained using a zoom lens and extension tubes.

A 5-W, argon-ion laser was used for flowfield illumination. The laser beam was first reflected on a concave mirror (diameter $\phi = 50$ mm, focal length $f = 1000$ mm) to obtain the desired thickness of the beam. The laser sheet was then obtained by reflecting this beam on a small mirror attached to a galvanometer scanner, which is a limited rotation servomotor that is specifically designed for highly linear torque and deflection characteristics. The resulting laser sheet had a thickness of about 3 mm. Silver-coated glass spheres with diameters ranging from 9 to 90 μm for high- and low-zoom levels, respectively, were used to obtain the proper flow seeding.

All of the experiments were conducted in a 152 × 152 mm (6 × 6 in.) water tunnel in the Aerospace Engineering Department. This small water tunnel has all of its test section sides made of transparent Plexiglas®. The length of the test section is 610 mm (24 in.). This facility has a maximum test section velocity of about 460 mm/s (1.5 ft/s) and a two-dimensional contraction ratio of 4 to 1.

IV. Sample Experiments and Results

For the purposes of software performance demonstration, simple two-dimensional flow experiments were run. Images were taken for two different configurations: a) boundary-layer flow and b) flow over a two-dimensional cylinder. Schematic representations of these configurations may be seen in Fig. 4. Case a was run with a freestream velocity of 21mm/s. As shown in Fig. 4a, the bottom of the image coincides with the floor of the test section. For this configuration, the

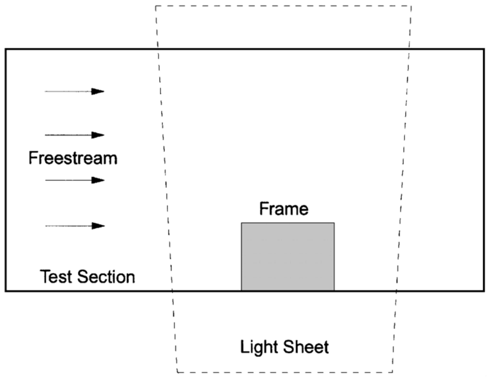

a) Boundary-layer flow

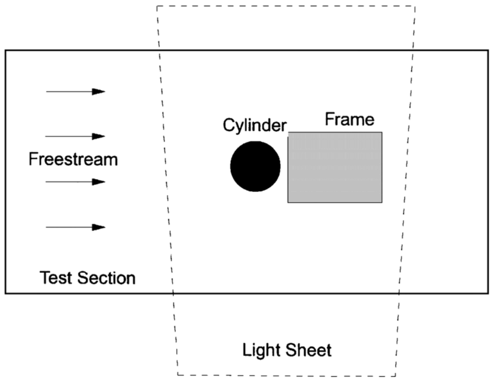

b) Flow over a two-dimensional cylinder

Fig. 4 Schematics of sample experiment configurations.

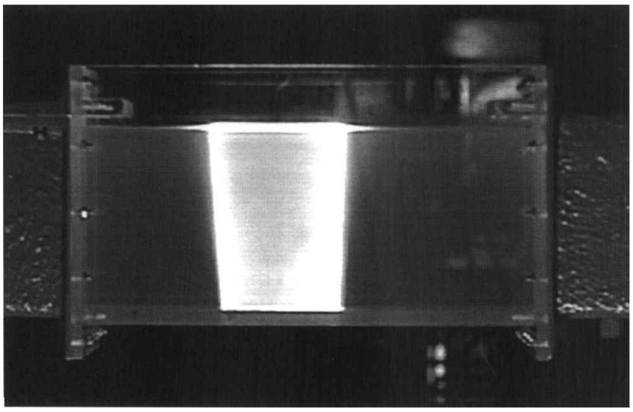

Boundary-layer flow

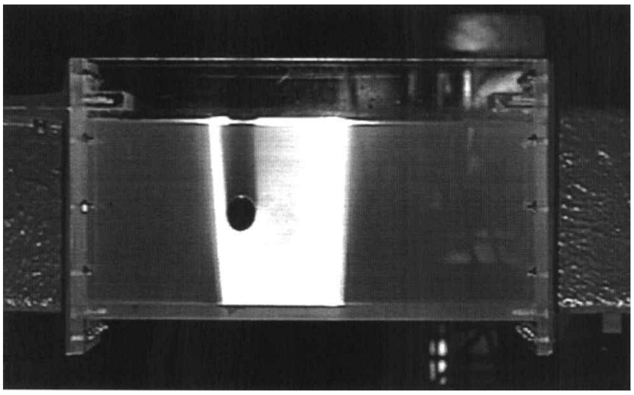

Flow over a cylinder

Fig. 5 Actual setups corresponding to the schematics of Fig. 4.

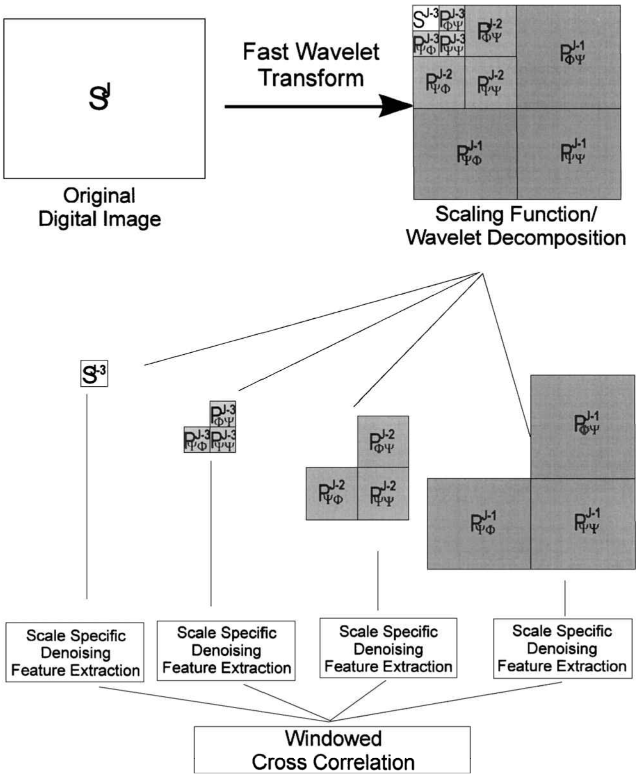

Fig. 6 Schematic of wavelet-based image processing method; three-level decompositions are shown.

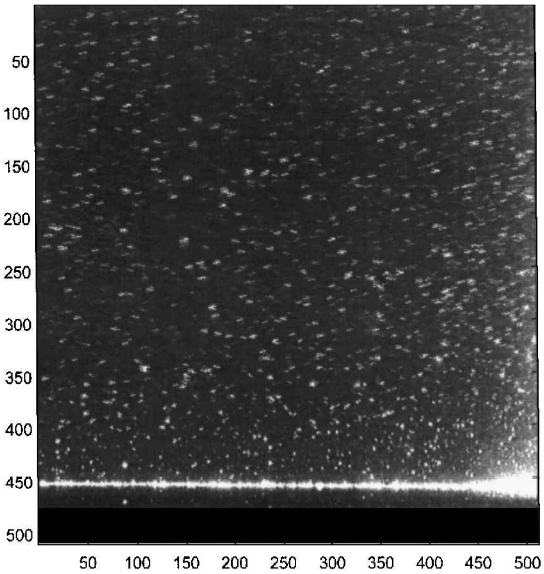

Fig. 7 Original particle image for the case of the boundary layer.

physical dimensions of the images were 31.75 × 38.1 mm (height × width). For case b, a cylinder with a diameter of 30 mm was placed with its center at a height of 75 mm from the tunnel floor. Images were captured for a freestream velocity of 44 mm/s. The physical dimensions of the images were 47 × 60 mm (height × width). To show the evolution of the fluid structures (vortex shedding) for the cylinder flow, image pairs were acquired with a user-defined time delay between each pair. The laser sheet and the location of the area that was captured in the image with respect to the cylinder and test section may be seen in Fig. 4. Figure 5 shows photographs of the actual experimental setup.

Figures 6–9 show the results of velocity field reconstruction from our simplest experiment (boundary layer) using the windowed, wavelet-based cross correlations derived in Sec. II.C. In Fig. 7, one of the two consecutive raw digitized particle images for the boundary-layer case is shown. Each frame is processed by utilizing the wavelet-based image processing method shown in Fig. 6. Each image undergoes a fast wavelet transform in two dimensions to obtain the projections onto the multilevel subspaces. By recalling the two-dimensional decompositions introduced in Eq. (14), the original image (S^J) is decomposed into the following multiscale representation (see Fig. 6):

$$\begin{aligned} S^J &= S^{J-1} + P^{J-1}_{\Phi\Psi} + P^{J-1}_{\Psi\Phi} + P^{J-1}_{\Psi\Psi} \\ &= \left(S^{J-2} + P^{J-2}_{\Phi\Psi} + P^{J-2}_{\Psi\Phi} + P^{J-2}_{\Psi\Psi}\right) + \left(P^{J-1}_{\Phi\Psi} + P^{J-1}_{\Psi\Phi} + P^{J-1}_{\Psi\Psi}\right) \\ &= \left(S^{J-3} + P^{J-3}_{\Phi\Psi} + P^{J-3}_{\Psi\Phi} + P^{J-3}_{\Psi\Psi}\right) + \left(P^{J-2}_{\Phi\Psi} + P^{J-2}_{\Psi\Phi} + P^{J-2}_{\Psi\Psi}\right) \\ &\quad + \left(P^{J-1}_{\Phi\Psi} + P^{J-1}_{\Psi\Phi} + P^{J-1}_{\Psi\Psi}\right) = \cdots\cdots \end{aligned} \tag{34}$$

where S are scaling components and P are wavelet components. The wavelet decomposition is split into parallel channels of wavelet coefficients, where each channel is associated with the detail images on a sequence of nested meshes. Each channel is denoised, via hard or soft thresholding, to retain only the relevant features at a given length scale. The resulting reconstructed, filtered image is used to calculate the windowed cross correlation via the expressions derived in Sec. II.C.

For example, Fig. 8 shows the results for the raw image (Fig. 7) when 1) the original image is decomposed to three multiresolution levels, 2) the coarsest data channel S^{J-3} is removed (no-pass filtering), and 3) all-pass filters are used for the detail images. This is perhaps the simplest multilevel filtering method conceivable for the PIV data: Retain only features corresponding to particles at the finest scales, and ignore all larger features. Figure 8a shows the image reconstructed from the finest level of details, i.e., $P^{J-1}_{\Phi\Psi} + P^{J-1}_{\Psi\Phi} + P^{J-1}_{\Psi\Psi}$. Figure 8b shows the image reconstructed from the next coarsest, i.e., $P^{J-2}_{\Phi\Psi} + P^{J-2}_{\Psi\Phi} + P^{J-2}_{\Psi\Psi}$, and so on. The coarsest level, i.e., $P^{J-3}_{\Phi\Psi} + P^{J-3}_{\Psi\Phi} + P^{J-3}_{\Psi\Psi}$, is shown in

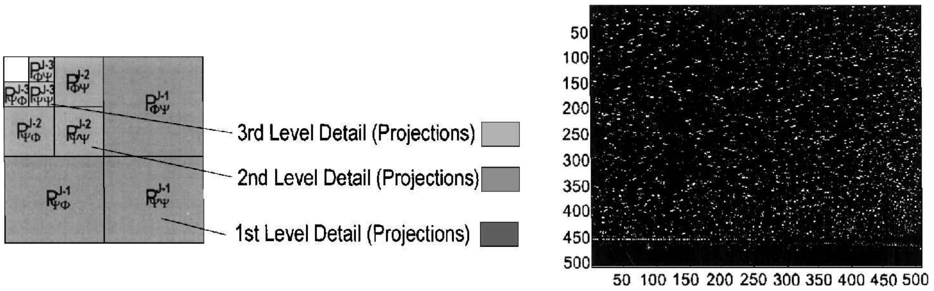

a) First-level detail

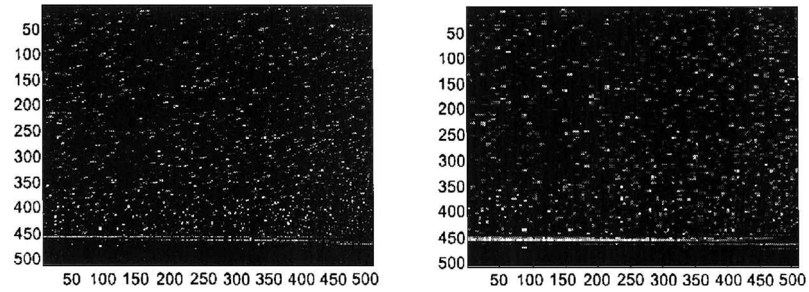

b) Second-level detail

c) Third-level detail

Fig. 8 Wavelet decomposition of the original image.

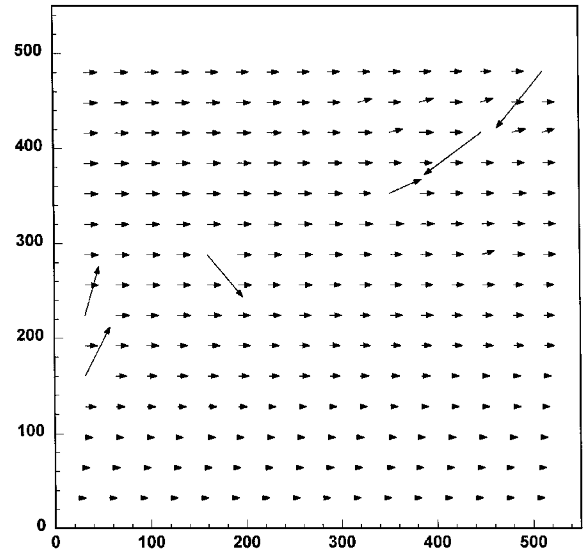

Fig. 9 Boundary-layer flowfield obtained through the wavelet-based cross correlation.

Fig. 8c. Despite only the most rudimentary filtering operation having been carried out in the feasibility study, excellent results are obtained. Figure 9 shows the velocity field that is reconstructed using the windowed cross-correlation expressions from Sec. II.C on the multiscale-filtered discrete wavelet transform. The size of the interrogation window for calculating the correlation function is fixed at 32 × 32 pixels throughout the experiment in this section. Only a few vectors are erroneously calculated out of 16 × 16 vectors, and most of them are located over regions of the image that contain data holes, i.e., low seeding particle density in the window. It is obvious that simple extrapolation, averaging, or flow-fitting procedures would eliminate these anomalies. We prefer to present the worst-case, raw data. It is emphasized that the displacement vector of the particles within the entire window is determined by simply finding the location of the maximum of the corresponding cross-correlation function without using any sophisticated algorithms. The vector describing the velocity is then calculated by simple division of the displacement by the time between consecutive images, i.e. the reciprocal of the frame rate of the CCD camera.

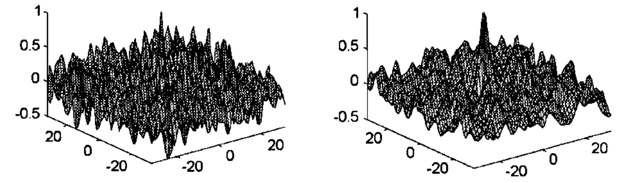

Two-level details

Four-level details

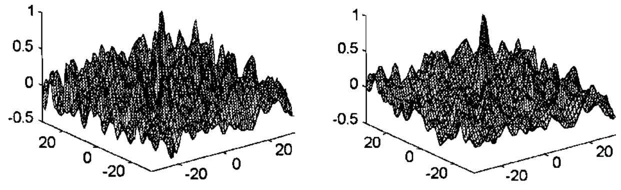

Three-level details

Five-level details

Fig. 10 Typical correlation measures for different wavelet filtering.

More challenging examples are presented in Figs. 10–13 for the representation of velocity fields of a cylinder wake. The same windowed, wavelet-based correlation algorithm is used as before. The multiresolution decompositions of the original images are performed up to five resolution levels to exhibit the effects of the number of levels of detail images retained. Typical correlation measures for different wavelet decomposition levels are shown in Fig. 10. It can be immediately seen that, as we keep more details, we obtain more distinct peaks in the correlation distribution. This procedure corresponds to the physically intuitive use of what we know about the physics of the flow; only small-scale particles are of interest. The large-scale features in this application can be discarded to produce improved results. This cleaner peak in the correlation in turn results in a reduced number of erroneous vectors, as can be seen in Fig. 11. The deletion of the large-scale features, i.e., coarsest components S^{J-5}, improves denoising, whereas retaining the finest-scale features improves local correlation. For the purpose of comparison, a result from an existing fast Fourier transform (FFT)- based DPIV code is presented in Fig. 12. The comparison of the wavelet-based method in Fig. 11d and the FFT-based method in Fig. 12 is quite promising. Because only a small number of flow vectors are erroneous, we are able to remove those vectors by averaging neighboring reasonable vectors. Fewer than 10% of the vectors comprising the velocity field were modified by this averaging operation. The

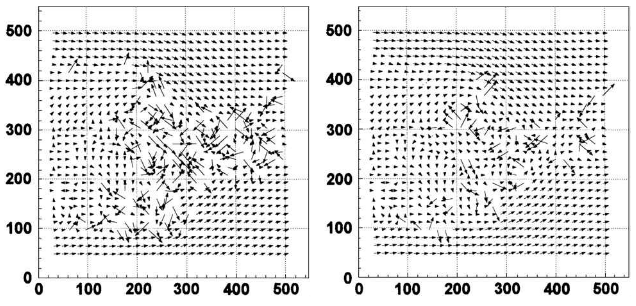

a) Two-level details **c) Four-level details**

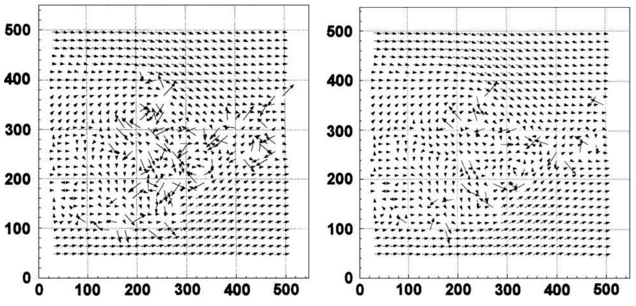

b) Three-level details **d) Five-level details**

Fig. 11 Velocity field computed for different numbers of levels of detail images retained.

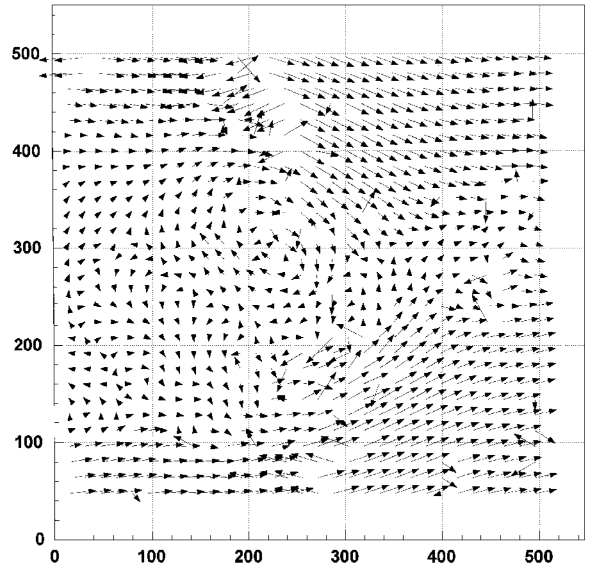

Fig. 12 Velocity field computed using original DPIV code.

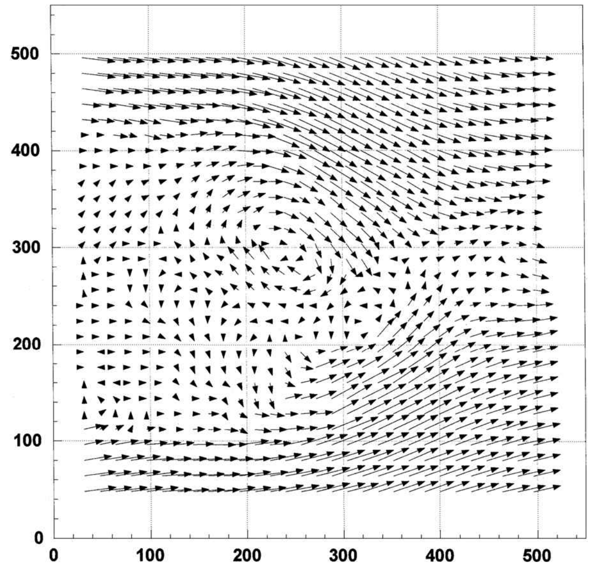

Fig. 13 Velocity field; five-level details, after cleaning.

cleaned version of this vector plot is shown in Fig. 13, and the original plot is shown in Fig. 11d.

V. Concluding Remarks

Novel analytical and image processing methods for DPIV have been presented. By deriving a windowed cross-correlation function for wavelet-based representations of CCD imagery, improved performance in terms of spatial resolution and reliability has been achieved. The derived method utilizes refinable functions to calculate local correlations, and fast computational forms have been derived and implemented. Wavelet-based denoising is employed to enhance spatial resolution. The techniques were applied to sample flowfields in water-tunnel experiments and showed excellent performance, demonstrating that simple, rudimentary wavelet filtering implementations yield results competitive with our best FFT-based methodologies.

Acknowledgments

This work was supported through the Advanced Research Program of the State of Texas under Grant 999903-180 and by the Association of American Railroads under Grant 95-39-RTD.

References

[1] Grant, I., and Liu, A., "Method for the Efficient Incoherent Analysis of Particle Image Velocimetry Images," *Applied Optics*, Vol. 28, No. 10, 1989, pp. 1745–1748.

[2] Keane, R. D., and Adrian, R. J., "Theory of Cross-Correlation Analysis of PIV Images," *Applied Scientific Research*, Vol. 49, No. 3, 1992, pp. 191–215.

[3] Willert, C. E., and Gharib, M., "Digital Particle Image Velocimetry," *Experiments in Fluids*, Vol. 10, 1991, pp. 181–193.

[4] Shimada, H., Murata, S., and Kise, H., "Particle Image Velocimetry Based on Fourier Transform Method for Measurement of Fluctuating Velocity Fields," *Transactions of Japanese Society of Mechanical Engineers*, Vol. 58, No. 552, 1992, pp. 2472–2478.

[5] Grant, I., and Qiu, J. H., "Digital Convolution Filtering Techniques on an Array Processor for Particle Image Velocimetry," *Applied Optics*, Vol. 29, No. 29, 1990, pp. 4327–4329.

[6] Nakatani, N., and Oshio, T., "Processing PTV Patterns by Holographic Correlation Technique," *Proceedings of the Seventh International Symposium on Flow Visualization*, Begell House, New York, 1995, pp. 746–751.

[7] Arnold, W., and Hinsch, K., "Purely Optical Parallel Processing in Particle Image Velocimetry and the Study of Flow Structures," *ICALEO '88, Optical Methods in Flow and Particle Diagnostics, Proceedings of the Laser Institute of America*, Vol. 67, Laser Inst. of America, Orlando, FL, 1988, pp. 157–165.

[8] Farrell, P. V., and Goetsch, D., "Optical Analysis of Particle Image Velocimetry Data," *ICALEO '89, Optical Methods in Flow and Particle Diagnostics, Proceedings of the Laser Institute of America*, Vol. 68, Laser Institute of America, Orlando, FL, 1989, pp. 82–91.

[9] Coupland, J. M., and Halliwell, N. A., "Particle Image Velocimetry: Rapid Transparency Analysis Using Optical Correlation," *Applied Optics*, Vol. 27, No. 10, 1988, pp. 1919–1921.

[10] Grant, I., and Liu, A., "Directional Ambiguity Resolution in Particle Image Velocimetry by Pulse Tagging," *Experiments in Fluids*, Vol. 10, No. 2/3, 1990, pp. 71–76.

[11] Adrian, R. J., "Image Shifting Technique to Resolve Directional Ambiguity in Double Pulsed Velocimetry," *Applied Optics*, Vol. 25, No. 21, 1986, pp. 3855–3858.

[12] Landreth, C. C., Adrian, R. J., and Yao, C. S., "Double Pulsed Particle Image Velocimeter with Directional Resolution for Complex Flows," *Experiments in Fluids*, Vol. 6, No. 2, 1988, pp. 119–128.

[13] Grobel, M., and Merzkirch, W., "White-Light Speckle Velocimetry Applied to Plane Free Convective Flow," *Experimental Heat Transfer*, Vol. 4, No. 3, 1991, pp. 253–262.

[14] Landreth, C. C., and Adrian, R. J., "Electrooptical Image Shifting for Particle Image Velocimetry," *Applied Optics*, Vol. 27, No. 20, 1988, pp. 4216–4220.

[15] Trump, D. D., Goss, L. P., and Gogineni, S. P., "Two-Color Particle Image Velocimetry Employing a Color CCD Camera," *Proceedings of the Seventh International Symposium on Flow Visualization*, Begell House, New York, 1995, pp. 622–627.

[16] Gilarranz, J., Singh, K., Ko, J., Rediniotis, O., and Kurdila, A., "High Frame-Rate, High Resolution Cinematographic Particle Image Velocimetry," AIAA Paper 97-0495, Jan. 1997.

[17] Vogel, A., and Lauterborn, W., "Time Resolved Particle Image Velocimetry," *Optics and Lasers in Engineering*, Vol. 9, No. 3, 1988, pp. 274–294.

[18] Chui, C. K., ed., *Wavelets: A Tutorial in Theory and Applications*, Academic, New York, 1992, pp. 181–216.

[19] Mallat, S., "A Theory for Multiresolution Signal Decomposition: The Wavelet Representation," *IEEE Transactions on Pattern Analysis and Machine Intelligence*, Vol. 11, No. 7, 1989, pp. 674–693.

[20] DeVore, R. A., and Lucier, B. J., "Image Compression Through Wavelet Transform Coding," *IEEE Transactions on Information Theory*, Special Issue on Wavelet Transforms and Multiresolution Signal Analysis, Vol. 38, No. 2, 1992, pp. 719–746.

[21] Shapiro, L. G., and Rosenfeld, A., *Computer Vision and Image Processing*, Academic, Boston, 1992, pp. 81–120.

[22] Daubechies, I., *Ten Lectures on Wavelets*, Society for Industrial and Applied Mathematics, Philadelphia, PA, 1992, pp. 1–52.

[23] Dahmen, W., and Micchelli, C. A., "Using the Refinement Equation for Evaluating Integrals of Wavelets," *SIAM Journal on Numerical Analysis*, Vol. 30, No. 2, 1993, pp. 507–537.

[24] Latto, A., Resnikoff, H. L., and Tenenbaum, E., "The Evaluation of Connection Coefficients of Compactly Supported Wavelets," Aware, Inc., TR AD910708, Cambridge, MA, July 1991.

[25] Ko, J., Kurdila, A. J., and Pilant, M. S., "A Class of Finite Element Methods Based on Orthonormal, Compactly Supported Wavelets," *Computational Mechanics*, Vol. 16, No. 4, 1995, pp. 235–244.

[26] Kunoth, A., "On the Fast Evaluation of Integrals of Refinable Functions," *Wavelets, Images, and Surface Fitting*, edited by P. J. Laurent, A. LeMehaute, and L. L. Schumaker, Peters, Boston, 1994, pp. 327–334.

G. M. Faeth
Editor-in-Chief